# Nanostructure and Oxidation of a Thin Film

## Ruthenium Molybdenum Alloy

ARCNL

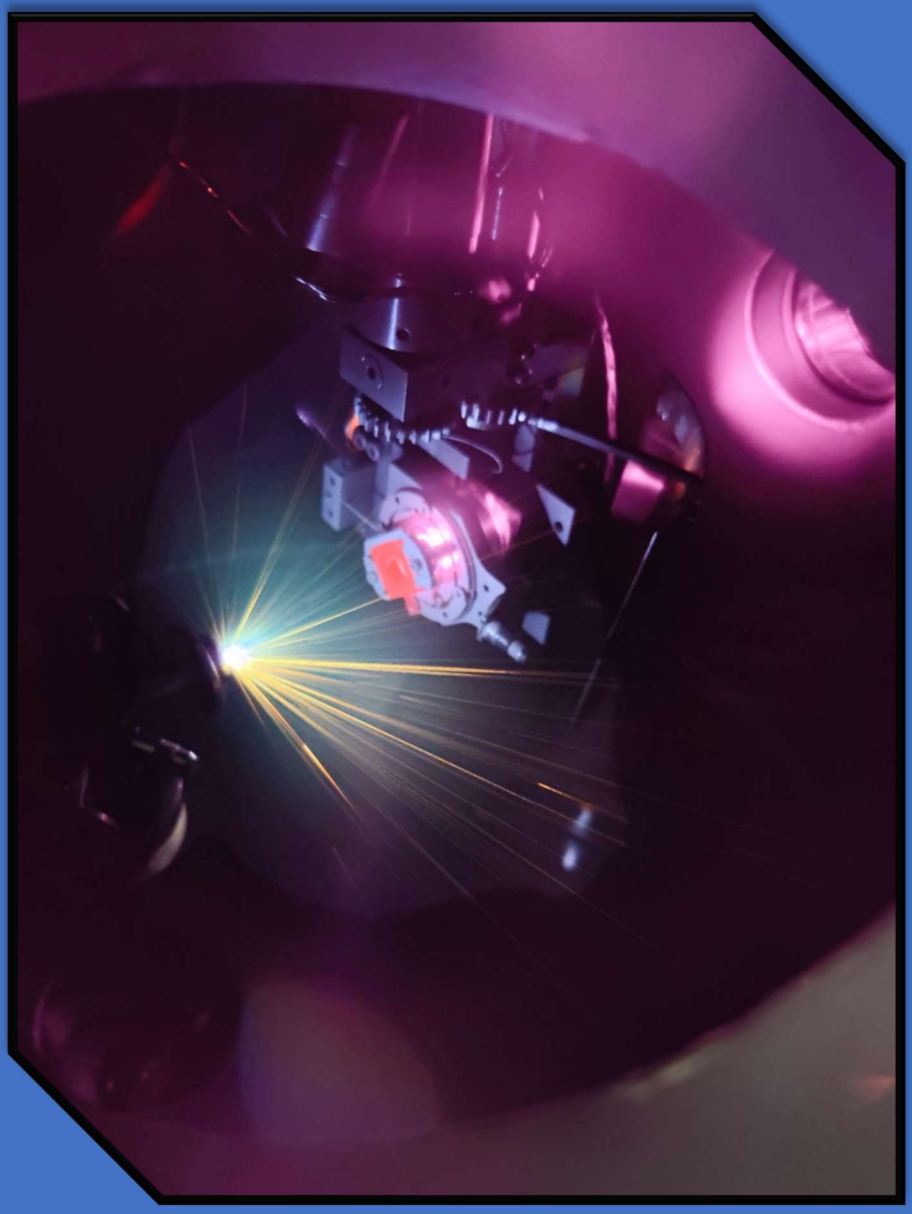

Bachelor Thesis Ruben Visser

**Bachelor Thesis Scheikunde**

# Nanostructure and Oxidation of a Thin Film

*Ruthenium Molybdenum Alloy*

*door*

**Ruben Visser**

23 December 2022

*Studentnummer*

11855207

*Onderzoeksinstituut*

ARCNL

*Onderzoeksgroep*

Materials & Surface Science for EUVL

*Verantwoordelijk docent*

Dr. Roland Bliem

*Begeleider*

Alessandro Troglia

## Abstract

The nanostructure and surface composition of a ruthenium molybdenum thin film deposited with pulsed laser deposition have been in investigated. This surface chemistry investigation focused on the interaction with oxygen and how the surface morphology influenced this interaction. Minimal difference in the amount of oxidation between a metallic glass and a polycrystalline film was observed. However, the ruthenium molybdenum thin film metallic glass showed promising properties regarding the surface roughness and oxide diffusion barrier characteristics.

## Samenvatting

In deze scriptie is onderzoek gedaan naar een nanomateriaal. Nanomaterialen zijn erg interessant binnen de high-tech industrie. Het gaat bij deze materialen om precisie om atoomniveau. Dat wil zeggen op de schaal van nanometers. Het onderzoek heeft zich gefocust op een superdun laagje gemaakt van de metalen ruthenium en molybdenum. Deze metalen zijn allebei essentieel voor het printen van de meest geavanceerde computerchips.

In het onderzoek is de focus gelegd op de structuur van dit laagje, en of die structuur invloed heeft op het oxidatie proces. De laagjes zijn gemaakt door middel van een techniek die Pulsed Laser Deposition heet. Deze techniek schiet een laser op een stukje metaal, in dit geval een legering van ruthenium en molybdenum. Het metaal wordt daardoor zo heet dat het een plasma vormt, dit lijkt op een gas, maar dan nog heter. Dit plasma kan je vervolgens opvangen op een klein glasplaatje zodat het weer een vaste stof wordt. Bij elk laser schot kunnen een paar atomen naar het glasplaatje verplaatsen, waardoor je dus met atomaire precisie een laagje kan vormen.

Metalen vormen normaal gesproken een kristalstructuur wanneer ze in vaste vorm zijn. Door de temperatuur van het glasplaatje op kamertemperatuur te houden bij PLD koelen de atomen zo snel af dat ze direct een vaste stof worden. Dit gaat dan zo snel dat ze geen tijd hebben om zich naar die kristalstructuur te oriënteren. Als je het glasplaatje echter verwarmt is er wel genoeg tijd voor de atomen om in die kristalstructuur te komen, omdat het plasma minder snel afkoelt. Op deze manier zijn twee verschillende laagjes van ruthenium en molybdenum gemaakt.

Er is vervolgens gekeken of deze laagjes op een andere manier reageren met zuurstof, maar het blijkt dat daar nauwelijks verschil in zit. Echter zit er wel een groot verschil in de nanostructuur van de laagjes. De ene is namelijk niet kristallijn en ook nog eens super vlak.

## Table of Contents

# 1 Introduction

## 1.1 Introduction

State-of-the-art technology, industrial equipment and household items can all benefit from materials with improved properties. Science and industry seek to develop smaller, more efficient, longer lasting, and better performing materials. Areas of interest in research for improving and tuning properties are nanocoating's and thin films. These nanomaterials can enable improved thermal, chemical, biological, optical, and mechanical behaviour compared to the bulk material underneath[1,2]. Thin films are essential for some processes such as computer-chip and display manufacturing, multilayer mirror production[3], and solar-cell production[4]. Due to the little material that is needed for the coating, it is often preferred to coat a substrate to enable certain surface properties compared to improving the properties of the substrate underneath. Besides functioning as a coating, thin films can also be used as a component to manufacture increasingly small products. Metal thin films are already widely used today, a film in this class of materials will be investigated in this report.

## 1.2 Thin film metallic glass

The use of thin metal films can be traced back to ancient Egypt where gold films were used as decoration and to preserve artifacts[5]. These films were found thousands of years later by archaeologists. This long lifetime is partly due to the excellent oxidation resistance these films have. With the introduction of sputter deposition in 1852 by Grove[5], a method was introduced utilizing vacuum equipment and vapor deposition; a method that is still used for modern applications. Research of thin metal films that have more resemblance to the film that will be investigated in this report started in the 1960's with early development of binary metallic glass (MG)[6].

MG is a term describing solid metals that lack the typical crystallinity and microstructures associated with metals produced with conventional methods[7]. For the formation of more than a few glass-forming alloys, the production method should be adapted. Pure metals or alloys can become amorphous if the cooling rate, when cooled from a non-solid phase, is sufficiently high. This lack in defined crystallization and absence of grain boundaries greatly influence the properties, often yielding improved mechanical, electrical and chemical attributes. However, these amorphous metals can also have downsides, the higher cost, limitations of production and loss of certain mechanical properties limit their application potential. So, in the right application these metals could be used to improve performance or resilience, but careful selection of the right materials requires advanced knowledge of the properties of these materials. Li et. al. reviewed recent developments for the application in electrocatalytic reactions, showing that the amorphous nature influences the chemical interactions of these metals[8]. In addition, Ashby et. al. concluded that for example micro-electronics, knife-edges, optics, and fashion items could all benefit from the properties enabled by MG[7]. Furthermore, this study also mentioned that MG can be deposited as thin film metallic glass (TFMG).

Properties and applications of TFMG have been reviewed by Chu et. al., who highlighted applications in display technology, memory devices, carbon-nanotube coatings and anti-microbial coatings[9]. The reviews mentioned above show that the fundamental physical and chemical principles, relevant for this class of

metal, are partly understood[7,8,9]. Moreover, many combinations of metals can potentially form a TFMG and all of those could have useful applications or enable innovations. However, not all physical and chemical properties have been investigated for those combinations and the fundamental principles that enable these properties are not fully understood. Thus, there is a great lack of knowledge in this field of science. One of these high-tech applications, dependent on innovations, is extreme ultraviolet lithography (EUVL). This process is used for producing the most advanced micro-electronics, operates in vacuum in a harsh environment and uses 13.5 nm radiation[10,11,12]. This manufacturing technique requires extreme precision and material resilience. The metals ruthenium and molybdenum have been found to be suitable metals for this application and both are already in use. They have advantageous properties regarding the interaction with EUV light and operation in vacuum. The harsh environment and atomic precision in the lithography process might provide a suitable application for a TFMG.

### 1.3 Ruthenium Molybdenum alloy

As discussed, alloys of ruthenium and molybdenum have recently received attention in science, but it appears the first investigations started in 1954, which investigated the crystal structure of the alloy[13]. Chemically, the elements have many similarities. Both are silvery second row transition metals only two atomic numbers apart, however there are differences. Ruthenium has a melting point of 2334 $C^o$, electron configuration of $[Kr]4d^7\ 5s^1$, and atomic radius of 2.13Å. While molybdenum has a melting point of 2623 $C^o$, electron configuration of $[Kr]4d^5\ 5s^1$, and atomic radius of 2.17Å. Moreover, ruthenium has an electronegativity of 2.2 (Pauling units), compared to 2.16 for molybdenum and they have very similar vaporisation enthalpies of 580 and 600 KJ $mol^{-1}$ respectively. Their crystal structure is not the same, simple hexagonal for ruthenium and a body-centered cubic structure for molybdenum. So, even though there are a lot of similarities in properties, how these elements behave in an alloy can be different. Take for example the crystal structure, when alloyed, it might take a different form. Moreover, the different melting points might greatly influence their behaviour during vapor deposition and the electronegativity could influence their reactivity.

In the 60's further experimental research expanded the knowledge of this alloy, showing that the melting point is $1945^o$+$10C^o$ for certain compositions[14]. It was also revealed that certain alloy compositions result in certain crystal phases. Namely, an alpha phase for molybdenum rich alloys, a beta phase for ruthenium rich alloys and a sigma phase that is present for the binary system with at least 10% to 60% molybdenum[15]. It was reported that this sigma phase has a pseudo hexagonal close packed structure, indicating that the alloy of these two elements have different nanostructures compared to their pure counterparts.

A more recent study investigated a sputter-deposited ruthenium molybdenum alloy TFMG and compared it to a polycrystalline counterpart[16]. It was proposed that due to the lack of crystallinity in the TFMG film, the properties could be improved. Grain boundaries were mentioned as the leading cause of change in properties. At these grain boundaries where the crystal structure is compromised, the atoms are more mobile, making the atoms in these boundaries more reactive. Moreover, the crystal grains usually do not align themselves perfectly, which causes some of the crystals to protrude above the surface more than other areas of the film. This was called the cobblestone effect, see figure 1. This effect would increase the surface roughness, expose deeper parts of the film, and reduces the general mechanical properties when compared to a single crystal or amorphous film.

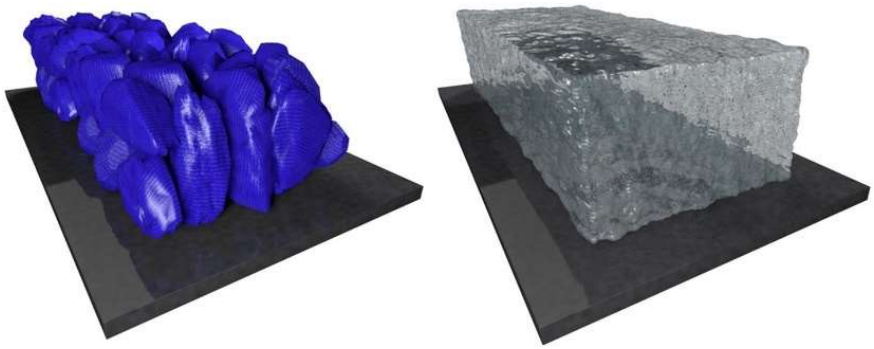

Figure 1: On the left, a visualization of the cobblestone effect in polycrystalline layers. On the right, the flatter and more homogenous structure of a TFMG[16].

The investigation by Yetik et. al.[16] concluded that sputter-deposition production of a ruthenium molybdenum TFMG was successful in a range of elemental compositions, from 35% to 50% ruthenium. Moreover, the films were relatively stable and flat compared to their crystalline counterparts, with an RMS roughness of approximately 0,26 nm. The improved properties were mainly attributed to the lack of grain boundaries. It was also discussed that the films, which had been exposed to air before measurements, contained some molybdenum oxide on the surface. This was concluded from analysis of XPS data. This data showed an increased amount of oxygen for films that contained an increased amount of molybdenum. An explanation for this was given, which is that ruthenium has a higher oxidation resistance. However, the oxidation process of the alloy was not investigated in detail. Pure ruthenium is known to have a high oxidation resistance and therefore is used as an oxidation resistant layer in some applications[17]. Comparatively, molybdenum has a lower resistance to oxidation and has been shown to fully oxidize to $MoO_2$ and $MoO_3$ under oxidizing conditions[18].

## 1.4 Research question

In this report the experiments and analysis that were performed to better understand the ruthenium molybdenum TFMG oxidation process will be described. In order to develop a better understanding of the stability and surface chemistry of this thin film this report will try to answer the following research question: *To what extent does the nanostructure influence the surface oxidation process of a ruthenium molybdenum thin film?*

## 1.5 Research structure

One of the experimental techniques that was used to answer the research question is Pulsed Laser Deposition (PLD). It is a similar technique to what was used by Yetik et. al.[16] for ruthenium molybdenum TFMG deposition. PLD, much like sputter-deposition, is a vapor deposition technique. It has been in use for more than 30 years and studied extensively[19]. The deposition process uses laser pulses to ablate material from a target. The energy at the ablation spot is tuned to be high enough to create a plasma cloud of stoichiometric composition. This plasma travels in a controlled environment towards a substrate where it cools and solidifies, see figure 2. Despite the relatively simple principle, PLD has many parameters

that can be tuned which include the laser wavelength, fluence, pulse duration, chamber gas composition and pressure, deposition distance, substrate temperature and substrate material. These parameters directly influence the properties of the deposited film. The interplay and effects of these parameters are complex but offer a method to reproduce complex film depositions with tuneable thickness down to the nanometer scale.

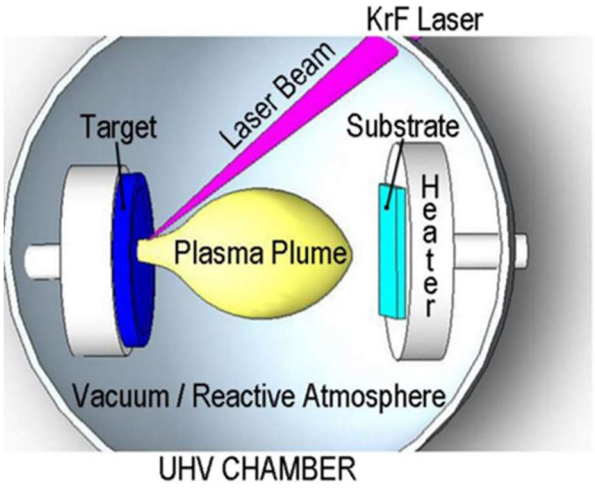


Figure 2: Schematic of the PLD system, reproduced form Gomez et. al.[20]

An essential parameter in the PLD process is the substrate temperature, this is used to control the cooling rate of the plasma. Depending on this cooling rate, the film can become amorphous or polycrystalline, as has successfully been shown by A. Troglia et al.[21]. In this case a binary alloy of CuZr was able to cool quick enough from plasma to solid so that it could form an amorphous thin film. The explanation for this behaviour is that the charged plasma particles lose their energy when arriving at the substrate. There needs to be sufficient energy and time to allow these particles to orient themselves in their preferred low energy crystal structure. If the particles are cooled fast enough, this atomic alignment is limited so a metastable amorphous material can be produced. For binary alloys the cooling rate should approximate $10^3$ K $s^{-1}$ or higher. For the ruthenium molybdenum system, it has not been confirmed if this required cooling rate can be achieved with PLD. So, during the research described in this report an effort was made to optimize the PLD parameters to produce an amorphous and polycrystalline ruthenium molybdenum thin film. The substrate temperature will be varied to induce a different nanostructure.

The goal of the optimization effort was production of two identical films that exclusively vary in their nanostructure. If there is a difference in surface oxidation behaviour that depends on the nanostructure this should then be observable. To verify the results of the optimization and analyse the oxidation behaviour, multiple measurements techniques were used. Atomic force microscopy and grazing incidence x-ray diffraction have been used to confirm the nanostructures and thickness of the produced films. For film composition and oxidation behaviour x-ray photoelectron spectroscopy (XPS) was utilized.

XPS is a surface analysis technique that can give information about approximately the first 10 nm of the surface[22]. By bombarding a sample with x-rays, the sample will emit photoelectrons with varying kinetic energies. The kinetic energy of these electrons can be measured and analysed to give information about the composition and chemical state of the atoms in the sample. Electron emission occurs when an x-ray

photon completely transfers its energy to a core level electron in the sample. The likeliness of this core level interaction is dependent on the element and x-ray source used. This effect is caused by the photoionization cross-section and should be compensated for in data analysis[23]. The kinetic energy of the emitted electron is also dependent on the element, this is the fundamental principle that is used for XPS characterization. Each core level electron that is emitted has a certain binding energy before emission which is dependent on the element, orbital and chemical state. So, by varying the x-ray energy and tracking the number of electrons emitted you can identify elements in a sample, while also getting information on the chemical state of these elements. Furthermore, the composition of the sample can be obtained when the data is analysed.

To observe the surface oxidation behaviour of the two optimized films, the surface composition can be analysed with XPS. For this process to be revealed, it was chosen to perform XPS on the samples at three stages. The first stage is the in-situ/pre-exposure stage when the samples should still have minimum oxidation due to continuous vacuum handling. Secondly, the quick-exposure stage allows for a relatively short interaction time between the sample surface and oxygen. And finally, a long-exposure stage that allows the samples to interact with oxygen for a longer time, this could give more insight in the oxidation process.

### 1.6 Reported sections

The following sections will address the used equipment for this research, experimental procedures and methodology. Subsequently, obtained results and measurements will be presented, starting with the results of the film optimization, followed by the surface oxidation investigation. These results will be discussed in context of the research question to get to a detailed conclusion. Finally, an appendix will be included so that the supporting information for the results can be presented.

# 2 Experimental

## 2.1 General experimental

### Equipment

- Sonication bath, HBM GL series 2.5 liter
- UHV Setup, Pfeiffer Vacuum turbo pumps
- PLD laser, Coherent COMPex 201 F (KrF 248 nm)
- Heater laser, Coherent (980 nm IR laser)
- Energy Sensor, Coherent, EnergyMax-USB J-50MUV-248 with Diffuser
- Pyrometer, SensorTherm GmbH, Metis M3
- XPS analyser, Scienta Omicron R4000 HiPP-3 (1 mm slit entrance, swift acceleration mode)
- XPS X-ray source, Al-Kα (1486.6 eV, monochromatic)
- AFM, Bruker Dimension Icon
- GI-XRD, Bruker D8 QUEST equipped with Incoatec IμS 3.0 CuKα x-ray source (λ = 1.5406 Å)
- XRD detector, PHOTON II Charge-integrating Pixel Array Detector (CPAD)

### Chemicals and Materials

- Sapphire (0001) crystal substrate, $Al_2O_3$ (Siegert Wafer GmbH)
- Acetone, $C_3H_6O$ (Biosolve, Cat. n:010305)
- 2-Propanol, $C_3H_8O$ (Biosolve, Cat. n:162605)
- Copper tape
- Photoresist
- Argon gas, Ar (Linde, 6.0 HiQ, ≥99,9999%)
- $Ru_{46}Mo_{54}$, ruthenium molybdenum alloy target (46+-1% Ru, 54+-1% Mo).
- Vacuum compatible sample holders (molybdenum, tantalum, steel)

## 2.2 Sample preparation

The films were deposited on the polished side of 5x5 mm sapphire (0001) ($Al_2O_3$) substrate in an ultra-high vacuum setup. The substrates were cleaned with first acetone and then isopropyl alcohol in an ultrasonic bath. After sonication, the substrates were dried with pressurized $N_2$ gas and mounted to a metal substrate holder using copper tape. For some samples, a small piece of copper tape was stuck on top of the sapphire substrate covering a small piece of the corner, while also contacting the metal sample holder. This was done to increase the conductivity of the surface after deposition. The copper tape was not used for the depositions at raised temperatures due to the adhesive in the tape being volatile at those temperatures, instead the substrate was secured on a tantalum plate with screws.

## 2.3 Ultra-high vacuum (UHV) handling

During deposition and XPS measurements the samples were encapsulated within an UHV setup with different chambers, load locks and transfer rods that could move the samples. The cleaned samples were placed in a load lock after which the load lock was pumped down to a vacuum. Within the entire vacuum setup, the pressure was continuously monitored and kept at low pressures not higher than $5.0*10^{-7}$ mbar. Average pressure in the setup was ~$1.0*10^{-9}$ mbar. However, during the depositions the pressure in the vacuum chamber was increased with a flow of argon gas for the duration of the deposition, this is described in detail in the deposition section.

## 2.4 Deposition procedure

The deposition took place inside of a UHV chamber. This chamber contained a movable sample holder, a movable target mount, and multiple windows. The 248 nm KrF laser, focused on the target, could enter the chamber through a specialized laser compatible window. If the target was moved out of the focus point the laser would travel through the chamber and out of another specialized window, where it could hit the EnergyMax energy sensor. Another laser compatible window located behind the sample holder was connected to 980 nm heating laser which focused on the back of the samples.

The sapphire substrates were secured at 55mm from the target alloy parallel to the flat surface of the target. The pressure was brought from a vacuum (~$1.0*10^{-9}$ mbar) to the required argon background pressure by continuously leaking argon into the deposition chamber during the deposition and pre-ablation. Before every deposition the ruthenium molybdenum target was cleaned by pre-ablating with laser pulses for >2 minutes (~1500 laser pulses). Durning cleaning, the target would be moving, this ensured that the laser would hit the entire surface of the target. Moreover, the substrate would be shielded during cleaning by a steel shield to prevent coating of the substrate before the start of the deposition. Before the start and after the deposition was complete, the energy of the KrF laser was measured at the window. The energy of the laser before entering the vacuum chamber was monitored to keep track of the transparency of the windows in the vacuum chamber, because the deposition process affects the transparency by coating the windows.

If the experiment required it, the heating laser would continuously be shooting at the back of the sample. The power of the heating laser (980 nm) would slowly be increased until the desired substrate temperature was reached. Substrate temperature was monitored with a pyrometer. The KrF laser ($0.4mm^2$ spot size, $45^o$ angle) would be set to shooting at 10 Hz and the target would continuously be moved when the deposition started. During deposition, the background pressure, total number of laser shots, and if applicable, substrate temperature would continuously be monitored to verify the correct deposition conditions.

When the required amount of laser shots was reached, the lasers and argon gas flow would be stopped. If needed, the sample was allowed to cool before transferring to the XPS setup.

## 2.5 X-ray photoelectron spectroscopy and data processing

XPS measurements of the films, taken before and after ambient exposure, were performed in an UHV setup. Samples were placed parallel to the 1 mm opening of the analyser, the distance between the sample and the opening was tuned for each sample to maximize the electron signal strength. In situ measurements were performed by transferring samples from the deposition chamber to the XPS chamber in vacuum. A pass energy of 500 eV was used for survey spectra, a pass energy of 100 eV was used for detailed spectra of ruthenium 3d, molybdenum 3d and oxygen 1s binding energy regions.

The XPS data was analysed with KolXPD (Kolibrik) software. The detailed (100 eV) spectra were fitted for elemental and chemical characterization. The fitting used Shirley functions for the background subtraction and Voigt functions for the peaks. The peak areas obtained from the fitting were used to calculate the elemental fractions. For the calculations the following photoionization cross sections were used: $\sigma_{Ru3d}$=0.172, $\sigma_{Mo3d}$=0.131, $\sigma_{O1s}$=0.04[23].

The equation is as follows:

$$x_i = \frac{\frac{A_i}{\sigma_i}}{\sum_{j=1}^{N}\left(\frac{A_j}{\sigma_j}\right)}$$

*Equation 1; x (fraction), A (Area),* σ (photoionization cross section), j (sum of all)

## 2.6 Ambient exposure of the films

To investigate the oxidation of the films, two methods were used for exposure to ambient conditions. A procedure named ‘quick exposure’ and one named ‘long exposure’; these will now be described starting with quick exposure.

A film that was deposited and analysed with XPS was transferred to a load lock in vacuum. Within the load lock the pressure would gradually be increased by first turning off the turbo pump attached to this load lack. When the turbo pump had come to a rest, the connection to the pre-pump was closed and a venting screw was opened. This stopped any gas from being pumped away from the load lock while ambient air could enter the chamber. The door of the load lock was unlocked, if the door opened it would indicate that the chamber was at ambient pressure. After 30 seconds, the door and the venting screw would be closed again while the connection to the pre-pump would be opened. This would start to lower the pressure again. Next, the turbo pump would be started to reach an ultra-high vacuum. This quick exposure process of increasing and lowering the pressure would take approximately 35 minutes.

The long exposure procedure would take the same steps as the quick exposure procedure with a longer time in ambient air. For the optimized samples ambient exposure was approximately two weeks. The samples would be taken out of the load lock, placed in a protective capsule, and stored. During these days AFM and XRD measurements were also performed on the samples.

### 2.7 Supporting methods*

The AFM system was placed in a soundproof chamber, set to PeakForce Tapping ScanAsyst mode and placed on top of a vibration isolated table. Subsequent processing of the AFM data was done with Gwyddion software. A thickness calibration was performed by applying a droplet of photoresist on the sapphire substrate before deposition of a film that used the optimized PLD parameters. This sample was washed with acetone in an ultrasonic bath after the deposition to remove the photoresist and partly expose the substrate. This allowed for measuring a height difference between the substrate and the ruthenium molybdenum surface with AFM.

X-ray diffraction measurements were performed on selected samples to investigate crystallinity. A grazing incidence setup was used to minimise the effect of the substrate on the measurements. The measurements were performed after the samples had been exposed to ambient conditions. The data was processed to produce an intensity vs. 2 theta graph, saturated pixels corresponding to outliers were removed from the diffraction patters in the appendix

*: These supporting methods have partly been performed in collaboration with a lab at VU Amsterdam University and a lab from another research group at ARCNL. The methods were performed in collaboration with Alessandro Troglia and Stefan van Vliet.

## 3 Results

Firstly, the film optimization stage will briefly be discussed in section 3.1. The results that were measured to confirm the effects of four deposition parameters will be presented, the corresponding data is available in the appendix. Secondly, the results for the films that were used in the oxidation experiments will be discussed in detail. This will include the nanostructure, composition, and oxidation process of the films.

### 3.1 Optimization

In the film optimization stage three deposition parameters were investigated. The laser fluence, the argon background pressure and the deposition duration. The effects were measured by XPS, AFM and GI-XRD. The laser fluence and Ar background pressure influenced the composition. First the laser fluence was investigated. A fluence of 8.0 J/cm$^2$ yielded a film composition of 45% Ru and 55% Mo, measured with XPS. Higher and lower fluences did not produce film compositions this closed to the target composition. Because of this result, all following depositions used a fluence of 8.0 J/cm$^2$

The argon background pressure did not have a significant influence on the ruthenium molybdenum ratio. However, it did affect the oxygen content. An argon background pressure of $2.0*10^{-2}$ mbar resulted in an oxygen content of 14%, measured with XPS. This was the lowest pressure that could be used in the experimental setup due to practical reasons. Increasing the argon pressure yielded films with oxygen content as high as 31%. So, an argon pressure of $2.0*10^{-2}$ mbar was used for the optimized films.

The thickness of a film produced with the optimized PLD parameters was calibrated with AFM. The height difference of the film and substrate was measured at three spots and found to be approximately 10 nm

after 20 minutes/12000 laser shots. This resulted in the optimized films being produced with 24000 shots to reach a thickness of approximately 20 nm.

The final growth recipe that was used to produce the two optimized films that have undergone the oxidation procedures are: 40 minutes (laser at 10 Hz) deposition duration, 8.0 J/cm$^2$ laser fluence and an argon background pressure of 2.0*10$^{-2}$ mbar. One of the films was deposited at room temperature and one of the films was produced with a substrate temperature of 680 C°. The full list of samples can be seen in table 1 in the appendix.

## 3.2 Film nanostructure

### Atomic Force Microscopy

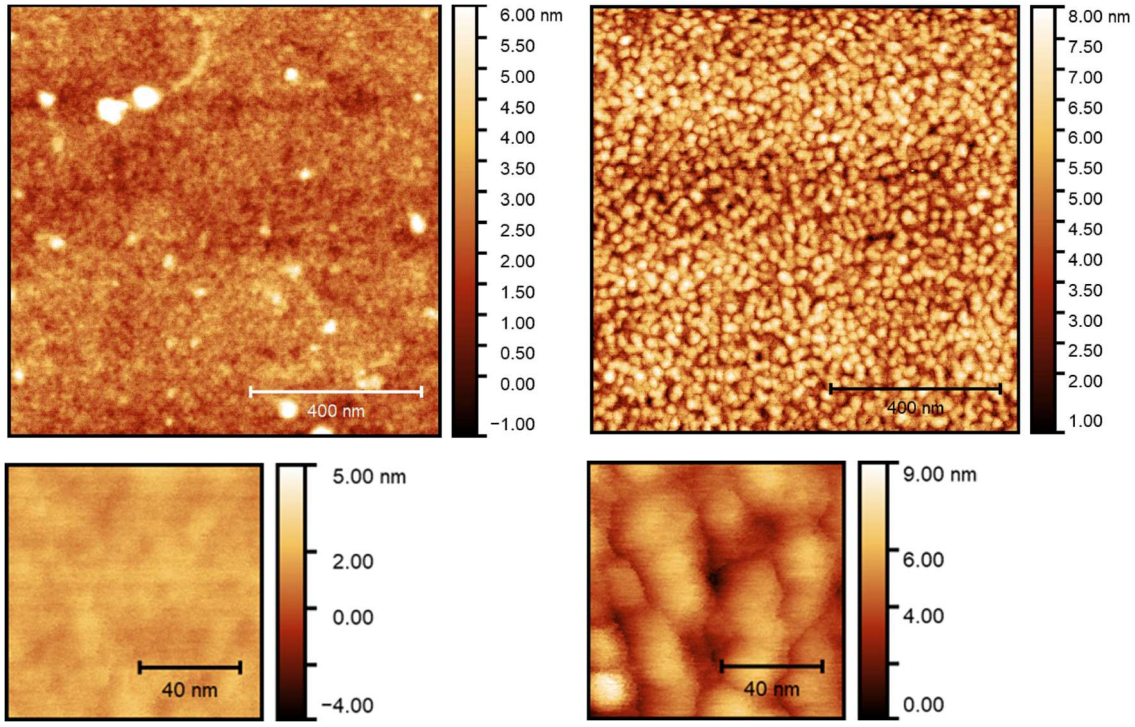


Figure 3: a) 1x1 µm height map of the sample produced with a room temperature substrate. The white spots show particles, likely molten RuMo droplets, that have made it to the surface during deposition. Besides these spots, the surface shows a high uniformity with most of the surface between 1.0 and 4.0 nm. b) 1x1 µm height map of the sample produced with a 680 C° substrate. Note that the height scale is the same as in image a. This image shows a rougher surface with most of the image using the full height scale of 1 nm to 8 nm. c) 100 x 100 nm height map of a surface spot within image a. This image shows a very uniform surface with a calculated RMS roughness of 0.389 nm. d) 100 x 100 nm height map of a surface spot within image b. This image shows a much rougher surface that resembles the cobblestone effect of figure 1. The calculated RMS roughness is 1.115 nm.

Grazing Incidence X-ray Diffraction

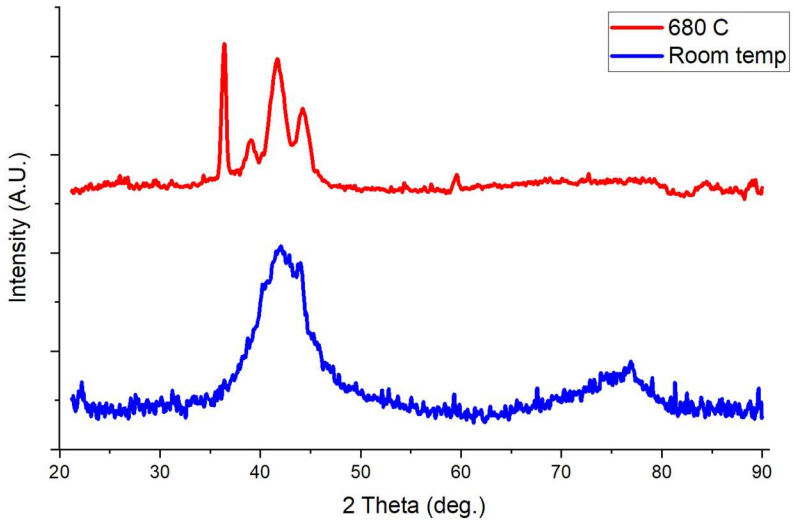


Figure 4: This graph shows the diffraction intensities for the films deposited on a room temperature substrate and a 680 C° heated substrate. The room temperature sample doesn't show well defined peaks. The broad peak around 40 degrees can be explained by a general similar bond distance between the ruthenium and molybdenum, however, there seems to be no clear crystallinity. In contrast, the red graph shows well defined crystal peaks at 36.45°, 39.05°, 41.75° and 44.20°. These can be attributed to $MoO_3$ and ruthenium[24,25].

3.3 Composition and Oxidation Process

As-deposited X-ray Photoelectron Spectroscopy

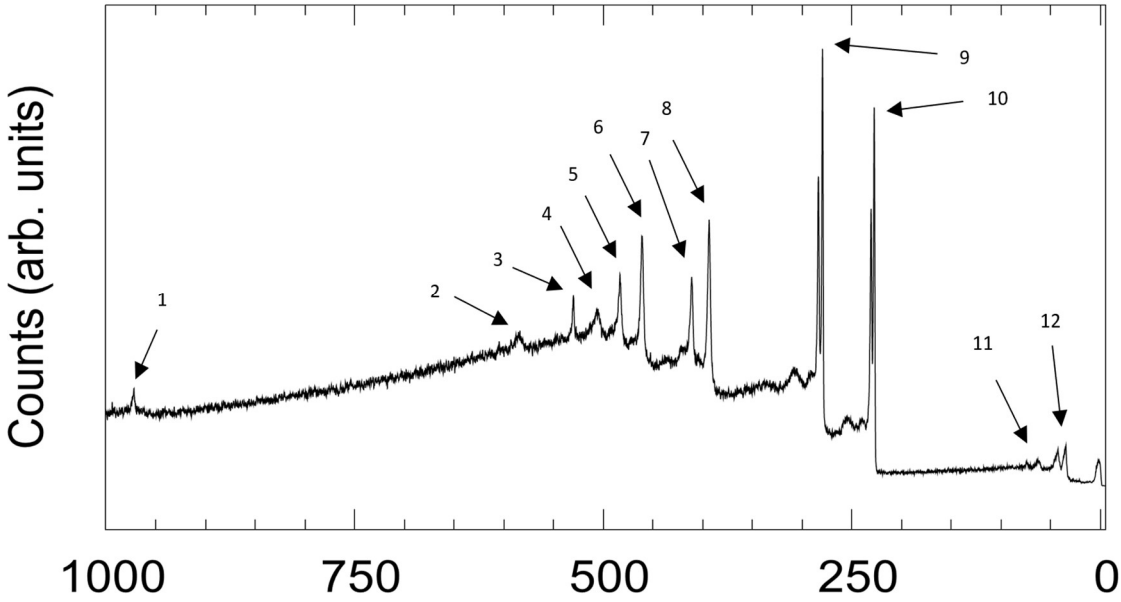


Figure 5: This figure shows the full XPS spectrum of an as deposited film on a room temperature substrate. This allowed for characterization of all present elements in the film. All peaks can be attributed to certain core electron signals[26]. (1) O KLL, (2) Ru3s, (3) O1s, (4) Mo3s, (5) Ru p1/2, (6) Ru p3/2, (7) Mo p1/2, (8) Mo p3/2, (9)Ru3d, (10)Mo3d, (11) Ru/Mo 4s, (12) Ru/Mo 4p. This lack of elements besides Ru, Mo, and O is consistent for all optimized films with one exception. This exception is a carbon peak that appeared in the long-exposed samples as will be discussed in the oxidation results.

Fitting of Detailed XPS Spectra

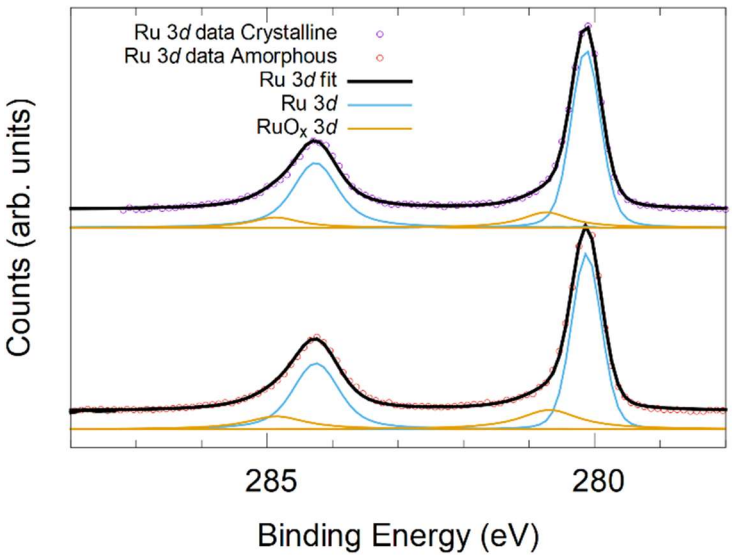


Figure 6: This figure shows an example of the fitting that was performed, in this case for the pre-exposure amorphous and crystalline samples. This detailed Ru 3d area shows negligible difference in terms of the Ruthenium species that are present in the two samples. This negligible difference is consistent for the Mo3d and O1s areas.

Composition of films before ambient exposure

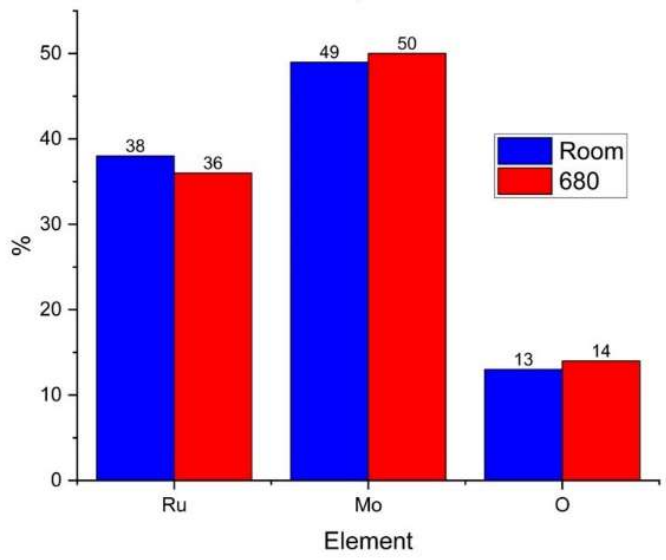


Figure 7: This graph shows the elemental composition of the two as-deposited films obtained from XPS fitting and calculations according to equation 1. This shows the depositions resulted in nearly identical film compositions before ambient exposure.

XPS fitting of the oxidation process for amorphous sample

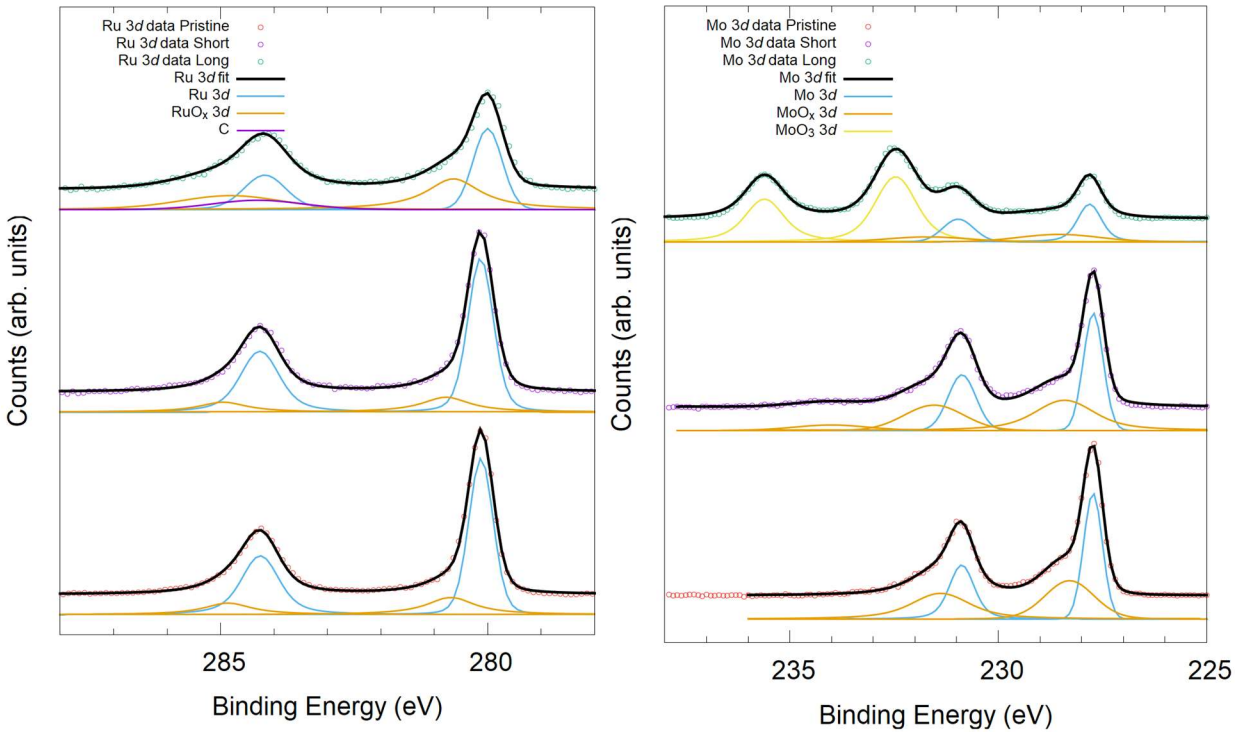


Figure 8: this figure show the detailed XPS spectra and fitting of the amorphous film in the Ru3d (left) and Mo3d (right) areas. The graph on the left shows that a significant increase in ruthenium oxide species is present after long exposure. Moreover, for a good fit a carbon 1s peak needed to be accounted for which is visible as the purple line. The graph on the right shows that there is a slight increase in and appearance of new molybdenum oxide species. For the long-exposed molybdenum region a completely different fitting shape is required. These peaks correspond to the binding energies associated with $MoO_3$. The general shape and progress in oxidation that is visible in these graphs is identical to the progress that can be seen in the crystalline sample, except for the long exposed Mo3d region. This difference can be seen in figure 9.

Mo3d region for long exposed amorphous and crystalline sample

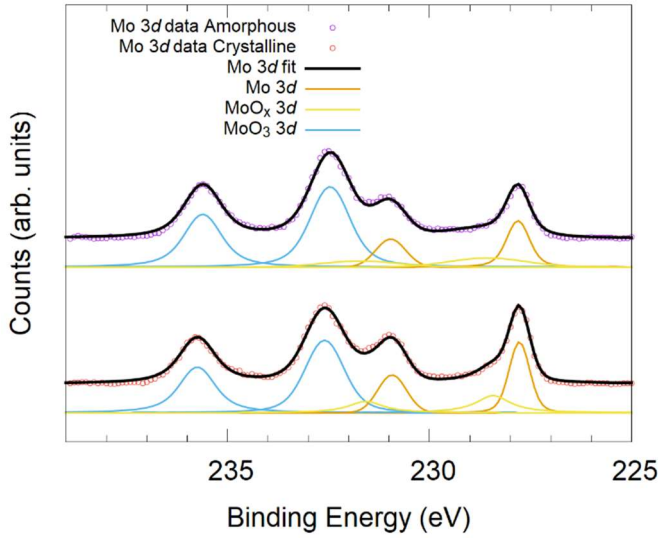


Figure 9: This figure shows the XPS fitting for the amorphous and crystalline sample in the Mo3d region. The oxide species that are present are the same and consist mostly of $MoO_3$. However, there is a noticeable difference in the unoxidized Mo peak. The crystalline sample shows a clear increased ration of the unoxidized metal.

Effect of Oxidation on Composition.

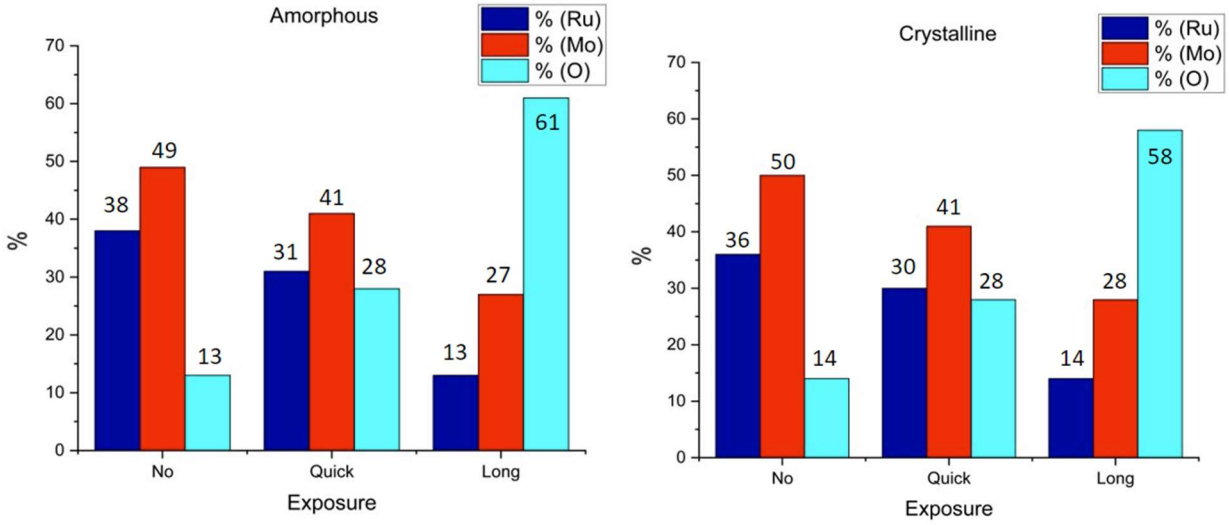


Figure 10: These two graphs show the compositional change during the oxidation process. These values were again calculated with equation 1 and the areas obtained by XPS fitting. This shows a nearly identical compositional change during the oxidation process.

# 4 Discussion

The optimization process described above yielded films of similar quality to what has been described in literature[16,21]. This was concluded by analysing the nanostructure and composition. Regarding the nanostructure, this was indicated by a relatively low surface roughness of 0.39 nm and a very similar surface topology compared to other TFMG materials. GI-XRD data in figure 4 provided the conformation that the optimized film deposited at room temperature was amorphous and the film deposited at higher temperatures showed clear crystallinity. Moreover, the thickness of ~40 nm was sufficient for proper decoupling of the substrate, meaning the thickness is more than the ~10 nm probing depth of XPS and sufficiently thick to produce a clear signal in GI-XRD.

The composition of the optimized films was nearly identical to the target alloy, only a slight enrichment in molybdenum was measured. The optimized films did not show contamination, besides the oxygen content, which was relatively low at 13/14%. All the peaks in XPS can be attributed to the metals or oxygen as is visible in figure 5. It was decided that the amount of oxygen was sufficiently low for the oxidation process to be measurable. Something worth noting is that it is difficult to conclude where this oxygen, present in the as-deposited films, originates from. The lowest oxygen content observed was 5%. This even lower oxygen content was measured on the same day as the deposition, something that usually was done on the next day due to relatively time-consuming procedures. Another likely explanation is that the target alloy already has native oxygen, unfortunately this oxygen contamination is not known for the target. Moreover, the optimization process also showed that leaking in the argon gas increased the amount of oxygen, so even at $2.0*10^{-2}$ mbar the background also contains oxygen. All these possible sources of oxygen make it hard to conclude how the oxygen content in the film before ambient exposure is caused, most likely it is a combination of all. However, the amount of oxygen in the films before exposure is sufficiently low for the oxidation process to cause a significant change. For this reason, in addition to nanostructure being the exclusive difference between the amorphous and crystalline film, the optimization was considered complete.

As mentioned, the GI-XRD data shows clear crystallinity with peaks that can be attributed to certain crystal phases. Namely the three Ru (100), (002), (101) peaks around $40^{o}$ were also found by Yetik et. al.[16]. However, comparatively the peaks in figure… have slightly shifted and broadened. This is to be expected because the molybdenum content in their RuMo films is 35% lower for the polycrystalline film. This means the inclusion of more molybdenum atoms in the ruthenium crystal structure causes the diffraction pattern to be slightly different. The other prominent XRD diffraction peak can be assigned to a molybdenum oxide. Both $MoO_2$ and $MoO_3$ have a peak at this angle, so it is difficult to conclude which species causes this peak from XRD data alone [24]. However, as will be discussed, this crystalline sample contains significantly more $MoO_3$ so it is very likely that this is a $MoO_3$ (012) peak.

The oxidation process for the quick and long exposures resulted in minimal variation between the amorphous and polycrystalline samples in terms of oxide content, as is clearly visible in figure 10. However, a slight deviation is ratios can be distinguished in figure 9. When comparing the fitted peaks for unoxidized Mo, the amorphous film has less unoxidized molybdenum at the surface. This indicates that the surface consists mostly of $MoO_3$. The amount of oxide species at the surface is also 3% more for the amorphous layer, the largest percentual atomic ratio difference between the two samples.

When putting this oxidation information in context, some interesting conclusions can be drawn. Most metals are known to form an oxide layer at the surface when given enough time. This oxide layer acts as

a barrier between the metal and gas, so further oxidation is limited[27]. To oxidize even further diffusion of the metal or the gas through this barrier must take place. However, if the barrier contains defects, the oxidation can happen rapidly. Now, when looking at the results in this report, both the amorphous and polycrystalline film have developed a diffusion barrier at the surface. However, due to the grain boundaries and roughness the quality of this barrier is compromised in the polycrystalline film. This phenomenon has been discussed for other binary amorphous metal alloys[28].

All in all, it seems a ruthenium molybdenum TFMG has many beneficial attributes, including a smooth surface, tuneable composition, ultra-thin deposition possibilities, and as described in this report, a superior diffusion barrier. The relatively simple investigation described in this paper has developed a deeper understanding of this material. However, some limitations should be discussed. To start, the ambient exposure procedure is simple, but not controlled. A better alternative might be to expose the samples to a controlled background pressure of pure oxygen in the UHV setup while tacking the oxidation with XPS. Moreover, a more detailed investigation into crystallinity could have been explored by annealing, which can induce crystallization. Unfortunately, the scope of this project did not allow for this. Other aspects that could have resulted in a more developed understanding include, depositing additional samples with different substrate temperatures or oxidizing the samples with a reactive liquid. Furthermore, more analysis techniques like electron microscopy or energy dispersive x-ray analysis could have given more insights in the oxidation process. Moreover, depositing a thin protective film on top of the samples before exposure would have allowed analysis of the films with XRD before any oxidation could influence the structure. An additional limitation is introduced due to the resolution depth of XPS. With the XPS method used, only speculation about what is happening beneath the first 10 nm of the surface is possible regarding the oxidation process.

# 5 Conclusion

The reported results clearly show that the films deposited at room temperature and at a raised temperature have a completely different nanostructures, but similar thickness. The film deposited at room temperature does not show crystallinity and has a low surface roughness, indicating that a TFMG structure was achieved. The film deposited at a high temperature shows clear crystallinity and a substantially higher surface roughness, indicating that a polycrystalline structure was achieved. This difference in nanostructure did not significantly influence the amount of oxidation on the surface. However, the nanostructure did influence the oxidation process, which was indicated by the formation of specific metal oxides that were found in varying ratios. Namely, the TFMG shows and increased ratio of $MoO_3$ at the surface, which is an indication of an improved oxide diffusion barrier.

# 6 Acknowledgement

During the research process I received great help and guidance by members of the Materials department at ARCNL. I especially want to thank Alessandro for the excellent supervision and answering of questions. Many thanks to Roland for giving me the opportunity to work on such a cool lab setup. Stefan, Tade and Ester also deserves a special thanks for their help in the lab.

# 7 References

(1) Singh, A.; Mittal, S.; Mudgal, D.; Gupta, P. Design, Development and Application of Nanocoatings. Advanced Structured Materials **2017**, 84, 191–207. https://doi.org/10.1007/978-981-10-6214-8_7.

(2) Mahapatro, A. Bio-Functional Nano-Coatings on Metallic Biomaterials. *Materials Science and Engineering: C* **2015**, *55*, 227–251. https://doi.org/10.1016/j.msec.2015.05.018.

(3) Bajt, S.; Chapman, H. N.; Nguyen, N.; Alameda, J.; Robinson, J. C.; Malinowski, M.; Gullikson, E.; Aquila, A.; Tarrio, C.; Grantham, S. Design and Performance of Capping Layers for Extreme-Ultraviolet Multilayer Mirrors. *Applied Optics* **2003**, *42* (28), 5750. https://doi.org/10.1364/ao.42.005750.

(4) Lira-Cantú, M.; Morales Sabio, A.; Brustenga, A.; Gómez-Romero, P. Electrochemical Deposition of Black Nickel Solar Absorber Coatings on Stainless Steel AISI316L for Thermal Solar Cells. *Solar Energy Materials and Solar Cells* **2005**, *87* (1-4), 685–694. https://doi.org/10.1016/j.solmat.2004.07.045.

(5) Greene, J. E. Tracing the 5000-Year Recorded History of Inorganic Thin Films from ∼3000 BC to the Early 1900s AD. *Applied Physics Reviews* **2014**, *1* (4), 041302. https://doi.org/10.1063/1.4902760.

(6) Klement, W.; Willens, R. H.; Duwez, P. Non-Crystalline Structure in Solidified Gold–Silicon Alloys. *Nature* **1960**, *187* (4740), 869–870. https://doi.org/10.1038/187869b0.

(7) Ashby, M.; Greer, A. Metallic Glasses as Structural Materials. *Scripta Materialia* **2006**, *54* (3), 321–326. https://doi.org/10.1016/j.scriptamat.2005.09.051.

(8) Li, J.; Doubek, G.; McMillon-Brown, L.; Taylor, A. D. Recent Advances in Metallic Glass Nanostructures: Synthesis Strategies and Electrocatalytic Applications. *Advanced Materials* **2018**, *31* (7), 1802120. https://doi.org/10.1002/adma.201802120.

(9) Chu, J. P.; Jang, J. S. C.; Huang, J. C.; Chou, H. S.; Yang, Y.; Ye, J. C.; Wang, Y. C.; Lee, J. W.; Liu, F. X.; Liaw, P. K.; Chen, Y. C.; Lee, C. M.; Li, C. L.; Rullyani, C. Thin Film Metallic Glasses: Unique Properties and Potential Applications. *Thin Solid Films* **2012**, *520* (16), 5097–5122. https://doi.org/10.1016/j.tsf.2012.03.092.

(10) Bajt, S. Molybdenum–Ruthenium/Beryllium Multilayer Coatings. *Journal of Vacuum Science & Technology A: Vacuum, Surfaces, and Films* **2000**, *18* (2), 557–559. https://doi.org/10.1116/1.582224.

(11) Mertens, B. Progress in EUV Optics Lifetime Expectations. *Microelectronic Engineering* **2004**, *73-74*, 16–22. https://doi.org/10.1016/s0167-9317(04)00066-8.

(12) Wood, O.; Raghunathan, S.; Mangat, P.; Philipsen, V.; Luong, V.; Kearney, P.; Verduijn, E.; Kumar, A.; Patil, S.; Laubis, C.; Soltwisch, V.; Scholze, F. Alternative Materials for High Numerical Aperture Extreme Ultraviolet Lithography Mask Stacks. *SPIE Proceedings* **2015**. https://doi.org/10.1117/12.2085022.

(13) Raub, E. *Zeitschrift Für Metallkunde*; **1954**, 45, 23-30

(14) Anderson, E.; Hume-Rothery, W. The Equilibrium Diagram of the System Molybdenum-Ruthenium. *Journal of the Less Common Metals* **1960**, *2* (6), 443–450. https://doi.org/10.1016/0022-5088(60)90026-6.

(15) Flewitt, P. E. J.; Tate, A. J. Some Structural and Physical Properties of "as Cast" Molybdenum-Ruthenium Alloys. *Journal of the Less Common Metals* **1972**, *27* (3), 339–352. https://doi.org/10.1016/0022-5088(72)90066-5.

(16) Yetik, G.; Troglia, A.; Farokhipoor, S.; van Vliet, S.; Momand, J.; Kooi, B. J.; Bliem, R.; Frenken, J. W. M. Ultrathin, Sputter-Deposited, Amorphous Alloy Films of Ruthenium and Molybdenum. *Surface and Coatings Technology* **2022**, *445*, 128729. https://doi.org/10.1016/j.surfcoat.2022.128729.

(17) Singh, J. P.; Karabacak, T.; Morrow, P.; Pimanpang, S.; Lu, T. M.; Wang, G.-C. . Preferred Orientation in Ru Nanocolumns Induced by Residual Oxygen. *Journal of Nanoscience and Nanotechnology* **2007**, *7* (6), 2192–2196. https://doi.org/10.1166/jnn.2007.793.

(18) Underwood, J. H.; Gullikson, E. M.; Nguyen, K. Tarnishing of Mo/Si Multilayer X-Ray Mirrors. *Applied Optics* **1993**, *32* (34), 6985. https://doi.org/10.1364/ao.32.006985.

(19) Singh, J. P.; Karabacak, T.; Morrow, P.; Pimanpang, S.; Lu, T.-M. .; Wang, G.-C. . Preferred Orientation in Ru Nanocolumns Induced by Residual Oxygen. *Journal of Nanoscience and Nanotechnology* **2007**, *7* (6), 2192–2196. https://doi.org/10.1166/jnn.2007.793.

(20) Gomez, C. L.; Ramirez, J. A.; Ordonez, J.; Ares, O.; Alvarado, J. J.; Champeaux, C.; Dumas, F.; Ezzahri, Y.; Joulain, K. Thermal Hysteresis Measurement of the VO2 Emissivity and Its Application in Thermal Rectification. *Scientific Reports* **2018**, *8* (1). https://doi.org/10.1038/s41598-018-26687-9.

(21) Troglia, A.; Vollema, V.; Cassanelli, S.; van Heumen, E.; van de Groep, J.; de Visser, A.; Bliem, R. Tuning Material Properties via Disorder: From Crystalline Alloy to Metallic Glass. *Materials Today Physics* **2022**, *29*, 100893. https://doi.org/10.1016/j.mtphys.2022.100893.

(22) Stevie, F. A.; Donley, C. L. Introduction to X-Ray Photoelectron Spectroscopy. *Journal of Vacuum Science & Technology A* **2020**, *38* (6), 063204. https://doi.org/10.1116/6.0000412.

(23) WebCrossSections https://vuo.elettra.eu/services/elements/WebElements.html (accessed 2022 -12 -20).

(24) Sheebha, I.; Vidhya, B.; Rajesh, S. Pulsed Laser Deposited Molybdenum Oxides ($MoO_3$ & $MoO_2$) Thin Films for Nanoelectronics Device Application. *4th International Conference on Devices, Circuits and Systems (ICDCS)* **2018,** 42-47. https://doi.org/10.1109/icdcsyst.2018.8605070.

(25) Singh, J. P.; Karabacak, T.; Morrow, P.; Pimanpang, S.; Lu, T.-M. .; Wang, G.-C. . Preferred Orientation in Ru Nanocolumns Induced by Residual Oxygen. *Journal of Nanoscience and Nanotechnology* **2007**, *7* (6), 2192–2196. https://doi.org/10.1166/jnn.2007.793.

(26) Moulder, J. F.; Chastain, J.; King, R. C. *Handbook of X-Ray Photoelectron Spectroscopy : A Reference Book of Standard Spectra for Identification and Interpretation of XPS Data*; Physical Electronics: Publisher: Eden Prairie, Minn., 1993.

(27) Stott, F. H. The Role of Oxidation in the Wear of Alloys. *Tribology International* **1998**, *31* (1-3), 61–71. https://doi.org/10.1016/s0301-679x(98)00008-5.

(28) Yang, J. J.; Yang, Y.; Wu, K.; Chang, Y. A. The Formation of Amorphous Alloy Oxides as Barriers Used in Magnetic Tunnel Junctions. *Journal of Applied Physics* **2005**, *98* (7), 074508. https://doi.org/10.1063/1.2084313.

**Appendix**

| Sample | Ru % | Mo % | O % | Ru/Mo | Fluence (J/cm²) | Ar P (mbar) | Temp (C°) | #laser shots |
|---|---|---|---|---|---|---|---|---|
| 1 | 33 | 44 | 23 | 42/58 | 9 | 0.04 | Room | 12000 |
| 2 | 33 | 42 | 25 | 44/56 | 10 | 0.04 | Room | 12000 |
| 3 | 34 | 46 | 21 | 43/57 | 8 | 0.04 | Room | 12000 |
| 4 | 30 | 39 | 31 | 44/56 | 8 | 0.1 | Room | 12000 |
| 4_exp | 8 | 20 | 72 | 29/71 | 8 | 0.1 | Room | 18000 |
| 5 | 39 | 47 | 14 | 45/55 | 8 | 0.02 | Room | 18000 |
| 5_exp | 17 | 24 | 59 | 42/58 | 8 | 0.02 | Room | 12000 |
| 6 | 37 | 49 | 15 | 43/57 | 8 | 0.02 | 560 | 24000 |
| 7 | 43 | 51 | 6 | 46/54 | 8 | 0.02 | 700 | 24000 |
| 8 | 30 | 40 | 30 | 43/57 | 8 | 0.1 | Room | 18000 |
| 9 | 34 | 62 | 5 | 35/65 | 8 | 0.02 | 700 | 24000 |
| 9_q_exp | 27 | 48 | 25 | 36/64 | 8 | 0.02 | 700 | 24000 |
| 10 | 38 | 49 | 13 | 43/57 | 8 | 0.02 | Room | 24000 |
| 10_q_exp | 31 | 41 | 28 | 43/57 | 8 | 0.02 | Room | 24000 |
| 10_l_exp | 13 | 27 | 61 | 32/68 | 8 | 0.02 | Room | 24000 |
| 11 | 36 | 50 | 14 | 42/58 | 8 | 0.02 | 680 | 24000 |
| 11_q_exp | 30 | 41 | 28 | 42/58 | 8 | 0.02 | 680 | 24000 |
| 11_l_exp | 14 | 28 | 58 | 34/66 | 8 | 0.02 | 680 | 24000 |

Table 1: All samples produced and their composition. _exp means it was exposed to ambient conditions before XPS measurement. Samples with _q_exp and _l_exp refer to the exposure procedures described in section 2.6. The samples 10 and 11 are the samples that are described as the optimized samples. Again, all these atomic ratios have been calculated with equation 1 and XPS fitting.

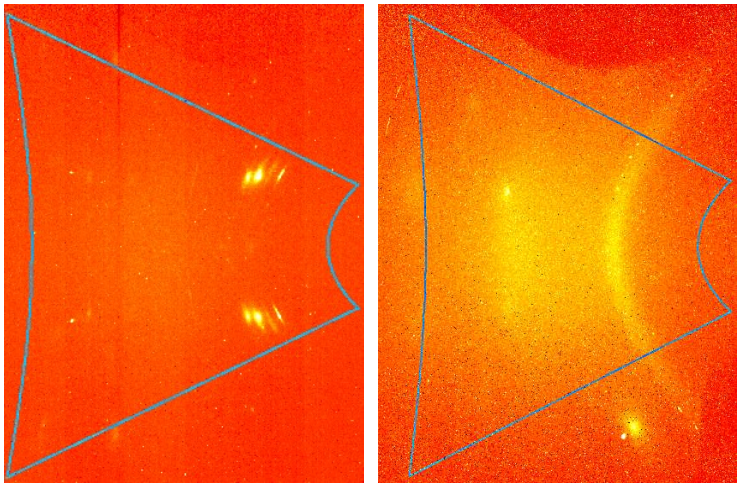

Figure 11: XRD raw data. On the left is the sample deposited at 680C° substrate, on the left room temperature substrate.